IEEE Access
Multidisciplinary : Rapid Review : Open Access Journal

Received March 30, 2020, accepted April 23, 2020, date of publication April 29, 2020, date of current version May 22, 2020.

Digital Object Identifier 10.1109/ACCESS.2020.2991148

Precise Internal Calibration Scheme for Very-High Resolution SAR System and Its Airborne Campaign Results

LI LI[1,2,3], MINGYI HE[1], FAN FENG[3], (Member, IEEE), AND CAIPIN LI[3]
[1]School of Electronics and Information, Northwestern Polytechnical University, Xi'an 710072, China
[2]National Key Lab of Science and Technology on Space Microwave, Xi'an 710100, China
[3]China Academy of Space Technology (Xi'an), Xi'an 710100, China

Corresponding author: Fan Feng (sailingvon@qq.com)

ABSTRACT For future ultra-high resolution spaceborne SAR missions, large beam-steering capability and large antenna aperture are demanded to increase the azimuth resolution and to maintain the sensor sensitivity simultaneously. Thus, large-deployable antenna is a desirable option as compared with planar array antenna for these missions, since it is advantageous in terms of mass, size, and cost. Moreover, its antenna pattern will not have any distortion with mechanical beam-scanning approach. In this paper, a novel reflector SAR system, including its platform configuration, attitude maneuvering strategy as well as SAR payload electronics are presented in detail. Furthermore, the key technique of very-high resolution SAR-internal instrument calibration scheme is also provided so as to remove the imbalance among channels to guarantee coherency and then to extract the range replica consequently. In the end, a carried-out airborne flight campaign is described and its imaging results are presented to validate the effectiveness of our system as well as calibration approach.

INDEX TERMS Synthetic aperture radar, very-high resolution, attitude maneuver, internal calibration, airborne campaign.

I. INTRODUCTION

As an active microwave imaging sensor, spaceborne synthetic aperture radar (SAR) has all-day and all-weather imaging capability, thus making it a very effective and efficient tool in both military and civilian Earth observation applications [1]–[5]. As one of its key performance figures, the finer the resolution becomes, the more details we can discern from the SAR image [6], [7]. In order to enhance two-dimensional resolution and guarantee SAR image quality simultaneously, three requirements, namely, 1) large transmit bandwidth in range, 2) large synthetic aperture in azimuth, 3) high effective isotropic radiation power (EIRP) have to be met [8]–[10]. Taking these demands into consideration, SAR antenna should have large aperture to increase its gain and be capable of beam-steering within large azimuth angles to improve the azimuth resolution. Besides, more information can also be retrieved from SAR images by multi-angle observation due to the mechanism of microwave scattering diversity [11]–[13].

Spaceborne SARs can be divided into two categories from the perspective of antenna. One is based on planar radiating array, while the other based on reflector [14]. For the first category, much research work has been done [15]–[17] due to the agility and convenience of its electronically beam-steering capability realized by phase-shifting in transmit-receive modules (TRMs), as explained in [18]. Nevertheless in case of large steering angle, electrical beam-scanning approach has severe shortcomings such as antenna gain degradation, presence of grating lobes, antenna pattern distortion and dispersion effect [19], especially for large bandwidth. And this will have significantly negative impacts on final SAR image quality. As a consequence, for SAR missions that should realize ultra-high resolution imaging and multi-angle observation, reflector SAR will be a more favorable alternative by virtue of its mechanical beam-steering manner, which will do no harm on antenna patterns. The observed region will always be illuminated by optimal antenna beam pattern

The associate editor coordinating the review of this manuscript and approving it for publication was Junjie Wu.

during the whole data take period, and thus more satisfactory performances can be achieved with regard to noise equivalent sigma zero (NESZ) and ambiguity-to-signal ratio (ASR), as compared to the planar array SAR.

To this day, reflector antennae have been successfully employed in SAR missions such as TECSAR [20], SAR-Lupe, and FIA for military reconnaissance; and also be the baseline for future BIOMASS, NISAR, TanDEM-L [21]–[23] civilian missions.

To gain more insights into ultra-high resolution reflector SAR and reap its benefits, we will bring forward an exemplary system and its key technique - internal instrument calibration scheme to make sure that range compression can achieve optimal results. Additionally, an airborne test campaign was carried out to verify the capability of reflector SAR in realizing high resolution and the effectiveness of suggested instrument calibration scheme.

The paper is organized as follows. Section II puts forward the exemplary reflector SAR system and describes its satellite configuration, attitude maneuvering strategy, and SAR payload electronics. In Section III, we propose the corresponding internal calibration scheme whereupon the associated operational flowchart and consequent processing algorithm are designed to realize the coherence of multiple channels and to extract the range compression replica. Section IV gives the airborne campaign results and makes a thorough quantitative analysis and discussion. The whole paper is concluded in Section V with a short summary.

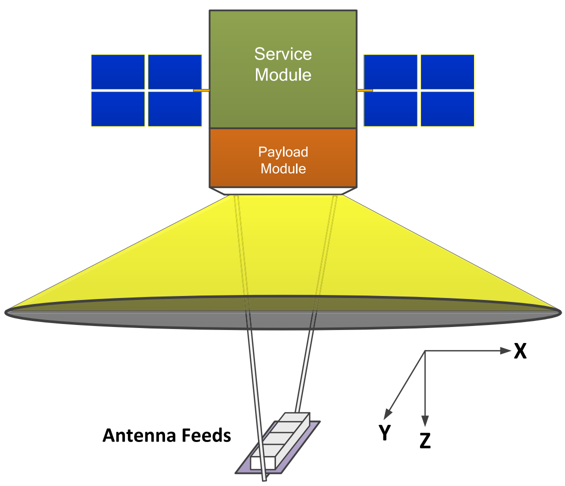

FIGURE 1. Ultra-high resolution reflector SAR satellite configuration.

II. ULTRA-HIGH RESOLUTION REFLECTOR SAR SYSTEM

A. SATELLITE PLATFORM CONFIGURATION

In order to realize the distortionless beam-steering with high agility and precision, single reflection umbrella-type antenna is selected as the SAR antenna, as illustrated in Fig. 1. It is fixedly connected to the platform on its +Z side, and the overall satellite configuration is composed of service module (SM), payload module (PM), and SAR antenna from up to down. The difference between satellite coordinate system and antenna counterpart only lies in their origin positions which are separated along the Z-axis. Antenna feeds are arranged on the topside of the antenna and connected to the SAR payload electronics by waveguides passing through the satellite board.

Antenna feeds are located on the focal plane and aligned to a single column in azimuth, and thus beam-steering in this dimension can only be achieved in a mechanical way by means of satellite attitude maneuvering. In range dimension, beam-scanning is realized via operational feeds switching which corresponds to different antenna beams illuminating different subswaths.

Compared with other reflector SAR satellites, such as TanDEM-L with ring truss cable net antenna or SAR-Lupe with solid surface reflector antenna, this satellite configuration makes an optimal tradeoff between antenna gain and platform agility to realize high resolution imaging of high quality. And the whole satellite structure can be rigid enough to adapt to the agile attitude maneuvering without causing serious reaction effects on platform, thereby ensuring the precision of beam pointing.

B. ATTITUDE MANEUVERING STRATEGY

In order to reduce the complexity as well as to guarantee the precision of SAR imaging processing, signal property of echoes in range and azimuth dimension should be decoupled from each other as much as possible. This requirement imposes certain demands on attitudes of the satellite platform as suggested in our work [24] and they are outlined as follows.

During the data acquisition period of ultra-high resolution imaging, +Z-axis of the platform should always be pointed to the virtual or real rotation center in case of sliding or staring spotlight mode, respectively. And its unit vector $\vec{\mathbf{E}}_z(t)$ can be expressed as

$$\vec{\mathbf{E}}_z(t) = \frac{\left(\vec{\mathbf{O}}_{\text{rot}} - \vec{\mathbf{P}}_{\text{sat}}(t)\right)}{\left|\vec{\mathbf{O}}_{\text{rot}} - \vec{\mathbf{P}}_{\text{sat}}(t)\right|} \tag{1}$$

where $\vec{\mathbf{O}}_{\text{rot}}$ is the coordinate of the rotation center, $\vec{\mathbf{P}}_{\text{sat}}(t)$ the satellite position and t the azimuth time variable.

Secondly, +Y-axis should be normal to the plane jointly determined by the +Z-axis and platform velocity vector $\vec{\mathbf{V}}_{\text{sat}}(t)$, and its unit vector $\vec{\mathbf{E}}_y(t)$ is thus given by

$$\vec{\mathbf{E}}_y(t) = \frac{\vec{\mathbf{E}}_z(t) \times \vec{\mathbf{V}}_{\text{sat}}(t)}{\left|\vec{\mathbf{E}}_z(t) \times \vec{\mathbf{V}}_{\text{sat}}(t)\right|} \tag{2}$$

Lastly, the unit vector of +X-axis $\vec{\mathbf{E}}_x(t)$ can be deduced from $\vec{\mathbf{E}}_y(t)$ and $\vec{\mathbf{E}}_z(t)$ by the right-hand rule as

$$\vec{\mathbf{E}}_x(t) = \vec{\mathbf{E}}_y(t) \times \vec{\mathbf{E}}_z(t) \tag{3}$$

With the attitude maneuvering strategy stated above, Doppler frequency of echoes can be kept almost unchanged along the range line for each azimuth position. Thus, the processing

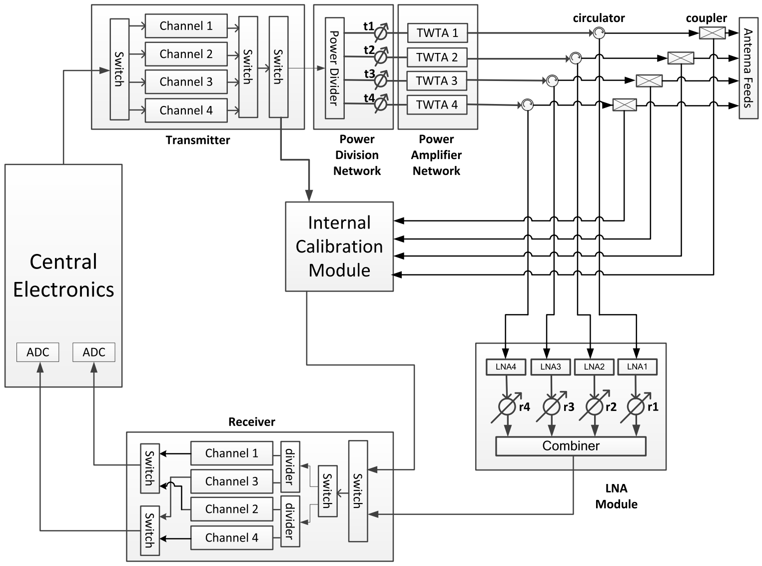

FIGURE 2. System block diagram of SAR payload electronics.

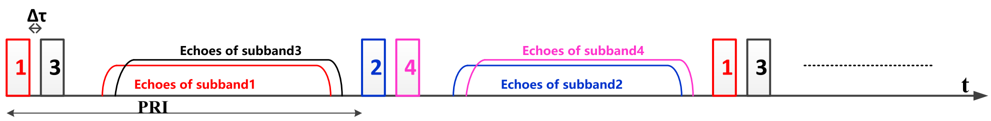

FIGURE 3. Pulse transmission sequence in the exemplary SAR system, where $\Delta\tau$ denotes the time interval between two adjacent subpulses.

algorithm will become much more efficient since each step of its workflow needs to deal with only one dimension and it can be carried out in a batch mode.

C. PAYLOAD ELETRONICS

The overall block diagram of SAR payload electronics is shown in Fig. 2. On system level, it can be divided into three blocks as 1) transmit path, 2) receive path, and 3) internal calibration loop. And all of them contain the transmitter, receiver as well as central electronics (CE).

Due to the sampling rate constraints of digital-to-analog converter (DAC) and analog-to-digital converter (ADC), both transmitter and receiver are equipped with multiple channels in parallel, each of which accommodates one sub-band (In this exemplary system, we assume $M = 4$ subbands). And channel switching is performed by fore and aft electronic switches within them, as illustrated in the diagram of these two parts.

In transmit path, the output of transmitter will firstly be passed through power division network (PDN) which consists of a power divider and N (Taking $N = 4$ as example) phase-shifters as represented by t1-t4. In the PDN, the radio frequency (RF) transmitted signal will be divided into N parts evenly, and their phases then be adjusted via phase-shifters to realize the coherence among them. The power amplifier network (PAN) is composed of N transmit wave tube amplifiers (TWTA), each of which performs the power amplification for each output of PDN. At last, these N high power signals will go through circulators and couplers sequentially to arrive at antenna feeds finally.

In receive path, low noise amplifier (LNA) module will perform the receiving with low noise, phase-shifting by r1-r4 and combination of echoes from 4 feeds. And its output will then be channelized to the receiver, where it is down-converted to the intermediate frequency (IF) for readiness of sampling by ADC in the central electronics.

To make an optimal compromise between pulse repetition frequency (PRF) and pulse duration as far as system performance is concerned; two non-adjacent sub-bands are transmitted consecutively in one transmission period and the other two sub-bands in next, as illustrated in Fig. 3. During the receiving, echoes of two subbands will be partially overlapped in time and they will be separated to different channels in the receiver.

The internal calibration module (ICU), together with couplers after the circulators, will be utilized to acquire the phase and gain characteristics of each transmit and receive channel. Fig. 4 shows its interior from which one can see that it includes several switches to adjust signal flow directions to accommodate different calibration modes. Fiber Optic Delay Unit (FODU) will delay the receiving of calibration signal and guarantee that it does not overlap with high

TABLE 1. System loops of SAR imaging and calibration modes.

Mode	Signal route
SAR imaging	CE→TR→PDN→PAN→circulator$_{(p1\to p2)}$→coupler$_{(p1\to p2)}$→Antenna→coupler$_{(p2\to p1)}$→circulator$_{(p2\to p3)}$ →LNA→RE
Transmission Calibration	CE→TR→PDN→PAN→circulator$_{(p1\to p2)}$→coupler$_{(p1\to p3)}$→ICM$_{c\to r}$→RE
Receiving Calibration	CE→TR→ICM$_{t\to c}$→coupler$_{(p1\to p3)}$→circulator$_{(p2\to p3)}$→LNA→RE
Reference Calibration	CE→TR→ICM$_{t\to r}$→RE

*TR: transmitter; RE: receiver; Subscript c→r: coupler→receiver; t→c: transmitter→coupler; t→r: transmitter→receiver)

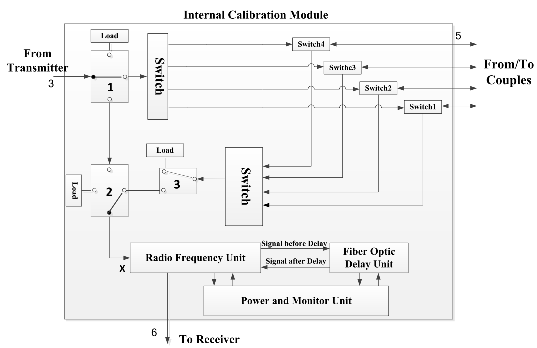

FIGURE 4. Interior of internal calibration module.

power transmission in time domain during transmission calibration, thereby avoiding the potential contamination from power leakage of PAN. The Radio Frequency Unit (RFU) is employed to fine-tune the signal power level to meet input requirements of FODU as well as that of receiver. Power and Monitor Unit is equipped to control the calibration module and acquire its state information.

The knowledge acquired by internal calibration will then be used to correct the imbalance among these channels and to extract the replica for range compression as described in next Section.

III. INTERNAL CALIBRATION

A. INTERNAL CALIBRATION LOOP AND WORKFLOW

Internal calibration involves three modes, namely transmission calibration, receiving calibration and reference calibration. The objective of first two modes is to obtain the phase and gain characteristics of power amplifiers and LNAs, respectively. And the last mode is employed to compensate common parts of the first two so as to make the final range replica to be identical to radar echoes as much as possible, whereupon the optimal compression results can thus be achieved.

For SAR imaging and calibration modes, system loops associated with them are listed in Table 1. Since circulators, couplers and ICM are all multi-port modules; their subscripts dictate the corresponding input and output ports, which are visibly annotated in Fig.5, associated with different modes.

Taking the 1st transmit-receive loop as an example, red lines in Fig. 6 shows the signal flow and corresponding switch settings within the ICM unit for all three calibration modes. Whereas in SAR imaging mode, all switches in the ICM will then be connected to the load to realize the highest isolation from the imaging route.

The overall internal calibration workflow is illustrated by the block diagram in Fig. 7. For each subband, it consists of channel imbalance correction, internal calibration posterior to it and the range replica construction in the end.

As aforementioned, the exemplary SAR system uses multiple parallel channels in PAN as well as LNA module; phase and amplitude imbalances between channels within each of them should be removed at first to realize coherent combination of signals in both transmit and receive path. For each subband, sine waves at the lowest, central and highest frequency within its spectrum are utilized to obtain the phase and amplitude differences between these channels. The corresponding results at these frequency points will then be averaged to evaluate the channel imbalance as a whole. During this procedure, signal routes are the same as that of transmission and receiving calibration shown in Table 1.

Based on imbalance knowledge obtained by the foregoing approach, attenuators and phase-shifters in both PDN and LNA module should then be tuned to compensate them. After this step, the internal calibration is performed to acquire the

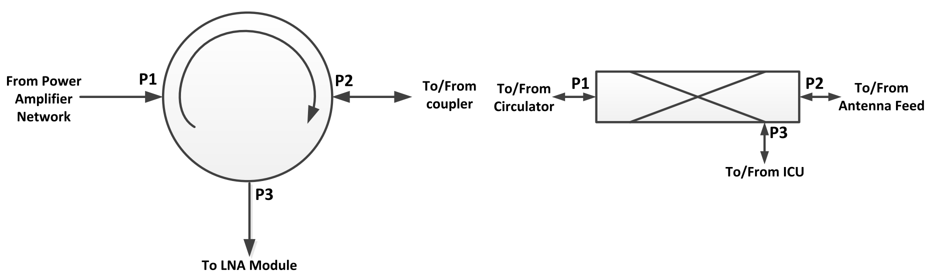

FIGURE 5. Input and output ports indices of circulator (left) and coupler (right).

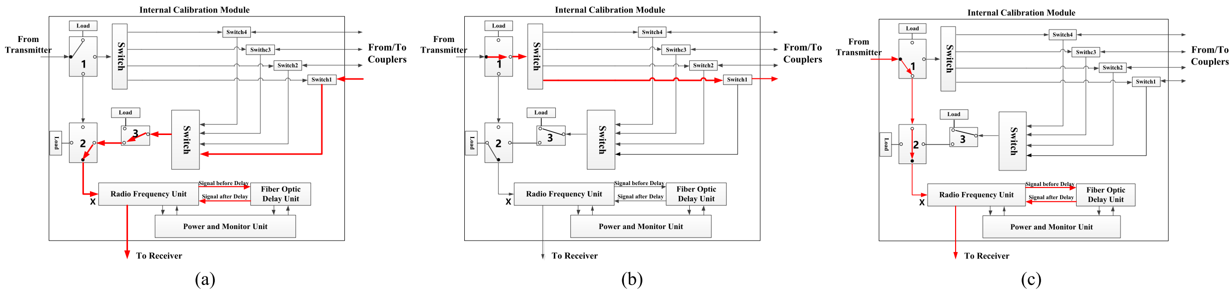

FIGURE 6. Signal flows in the ICM unit for (a) transmission, (b) receiving and (c) reference calibration modes.

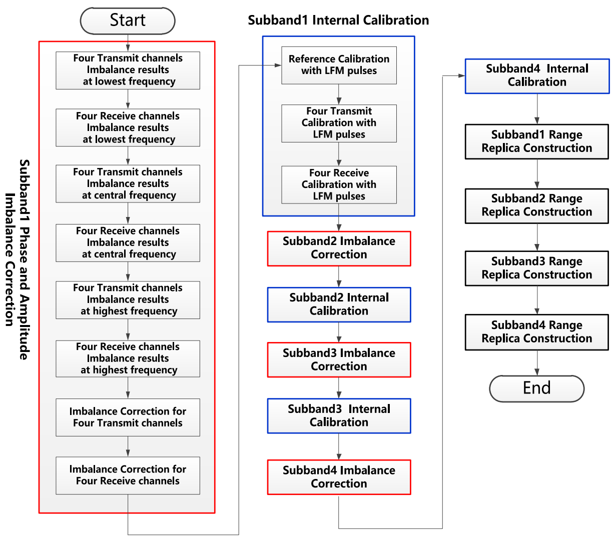

FIGURE 7. The overall internal calibration workflow.

TABLE 2. Symbols in transfer functions of calibration and imaging modes.

Symbol	Transfer function
Hk_T	the *k*th transmission calibration route
H_{ref}	the reference calibration route
Hk_R	the *k*th receiving calibration route
Hk_{sig}	the *k*th transmit-receive loop
H_{CE}	the central electronics
H_{TR}	the transmitter
Hk_{twta}	the *k*th power amplifier
$Hk_{cir1\text{-}2}$	port1→port2 of *k*th circulator
$Hk_{cir2\text{-}3}$	port2→port3 of *k*th circulator
$Hk_{coup1\text{-}2}$	port1→port2 of *k*th coupler
$Hk_{coup1\text{-}3}$	port1→port3 of *k*th coupler
$Hk_{coup2\text{-}1}$	port2→port1 of *k*th coupler
$Hk_{coup3\text{-}1}$	port3→port1 of *k*th coupler
$Hk_{c\text{-}r}$	the *k*th route in ICM from *k*th coupler to receiver
$H_{t\text{-}r}$	the route in ICM from transmitter to receiver
$Hk_{t\text{-}c}$	the *k*th route in ICM from transmitter to *k*th coupler
Hk_{LNA}	the *k*th route in the LNA module
H_{RE}	the receiver

range replica. One single internal calibration period consists of one reference, four transmission and four receiving calibration, which are performed in sequence, to cover all the four transmit-receive loops. The reason for this order is that both reference and transmission calibration pulses will go through

FIGURE 8. Airborne SAR antenna and its Servo control system mounted in the air pod.

TABLE 3. Airborne SAR system working parameters.

Parameter	Value
flight height	5000 m
flight velocity	120 m/s
looking angle in elevation	60°
PRF range	5000 Hz ~ 6600 Hz
azimuth scanning range	± 25°
subband1	8.285 GHz ~ 9.115 GHz
subband2	9.035 GHz ~ 9.865 GHz
subband3	9.735 GHz ~ 10.565 GHz
subband4	10.485 GHz ~ 11.315 GHz
reflector size	800 mm(A) × 300 mm(E)
focal length	300 mm

the FODU which has the linearly time-drifted phase property, thereby requiring that time interval between them be as short as possible. In this way, extra phase induced by FODU can be approximately considered as a common factor to both reference and transmission calibration signals, thus simplifying the range replica extraction. The internal calibration process will be repeated over many times to reduce the impact of Gaussian noise and improve the signal-to-noise ratio (SNR) of final replica.

B. ALGORITHM OF RANGE REPLICA EXTRACTION

In this subsection, the range replica extraction algorithm will be given on the basis of above internal calibration approach. According to signal routes of three calibration modes,

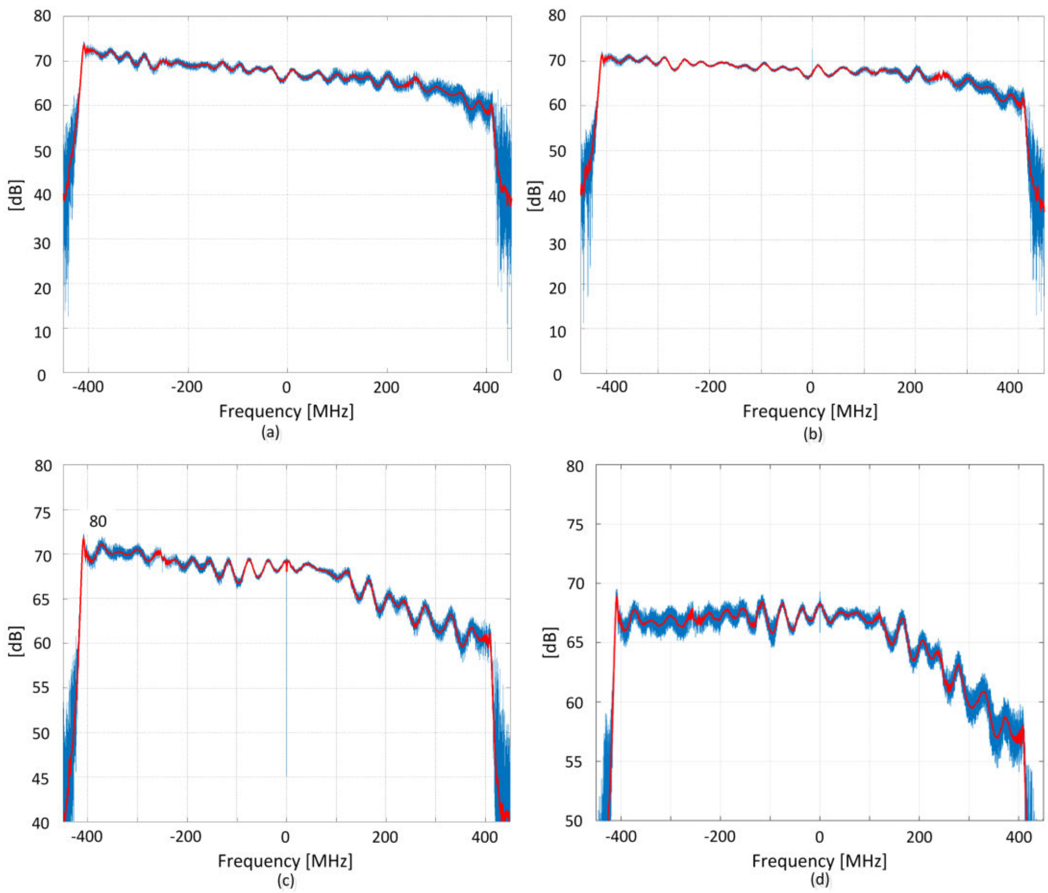

FIGURE 9. Amplitude frequency responses of term $Hk_T \cdot Hk_R/H_{ref}$ associated with four transmit-receive calibration channels for subband1.

their transfer functions can be explicitly expressed as

$$Hk_T = H_{CE} \cdot H_{TR} \cdot Hk_{twta} \cdot Hk_{cir1\text{-}2} \cdot Hk_{coup1\text{-}3} \cdot Hk_{c\rightarrow r} \cdot H_{RE} \tag{4}$$

$$H_{ref} = H_{CE} \cdot H_{TR} \cdot H_{t\rightarrow r} \cdot H_{RE} \tag{5}$$

$$Hk_R = H_{CE} \cdot H_{TR} \cdot Hk_{t\rightarrow c} \cdot Hk_{coup3\text{-}1} \cdot Hk_{cir2\text{-}3} \cdot Hk_{LNA} \cdot H_{RE} \tag{6}$$

As to the imaging mode, the transfer function of its *k*th transmit-receive loop (excluding antenna) is given by

$$Hk_{sig} = H_{CE} \cdot \left(H_{TR} \cdot Hk_{twta} \cdot Hk_{cir1\text{-}2} \cdot Hk_{coup1\text{-}2} \cdot Hk_{coup2\text{-}1} \cdot Hk_{cir2\text{-}3} Hk_{LNA}\right) \cdot H_{RE} \tag{7}$$

and annotations of these symbols used in above equations are listed in Table 2.

By comparing Eq. (4) ∼ Eq. (6) and Eq. (7), it can be seen that most sub-transfer functions of imaging mode are already embodied within that of calibration modes, except for a few ones. Therefore, Hk_{sig} can be expressed in terms of Hk_T, H_{ref} and Hk_R as

$$Hk_{sig} = \frac{Hk_T Hk_R}{H_{ref}} \cdot \frac{H_{t\rightarrow r}}{Hk_{c\rightarrow r}} \cdot \frac{1}{Hk_{t\rightarrow c}} \cdot \frac{Hk_{coup1\text{-}2} \cdot Hk_{coup2\text{-}1}}{Hk_{coup1\text{-}3} \cdot Hk_{coup3\text{-}1}} \tag{8}$$

Since all of four TWTAs as well as LNA units have been used for transmission and receiving respectively, the range replica could be given by the combination of four transmit-receive loops as

$$H_{sig} = H1_{sig} + H2_{sig} + H3_{sig} + H4_{sig} \tag{9}$$

From Eq. (8) and (9), it can be observed that besides Hk_T, H_{ref} and Hk_R, transfer functions associated with couplers as well as ICM are needed to derive the final range replica. Due to the passive microwave properties, transfer function of coupler is comparatively constant and will not vary significantly in orbit. Thus, it can be measured with the aid of vector network analyzer (VNA) beforehand. As regards to ICM properties, Hk_{t-c} only consists of switches and will perform stably onboard and can also be determined in advance. Nevertheless, properties of Hk_{c-r} and H_{t-r} will vary with time and operation circumstance, since RFU and FODU in their routes are all active modules. And this issue must be tackled carefully to guarantee the effectiveness of range replica.

To deal with this problem, we decompose the term $\frac{H_{t\rightarrow r}}{Hk_{c\rightarrow r}}$ in Eq. (8) further as

$$\frac{H_{t\rightarrow r}}{Hk_{c\rightarrow r}} = \frac{H_{switch} \cdot H_{RFU+FODU}}{Hk_{switch} \cdot H_{RFU+FODU}} \tag{10}$$

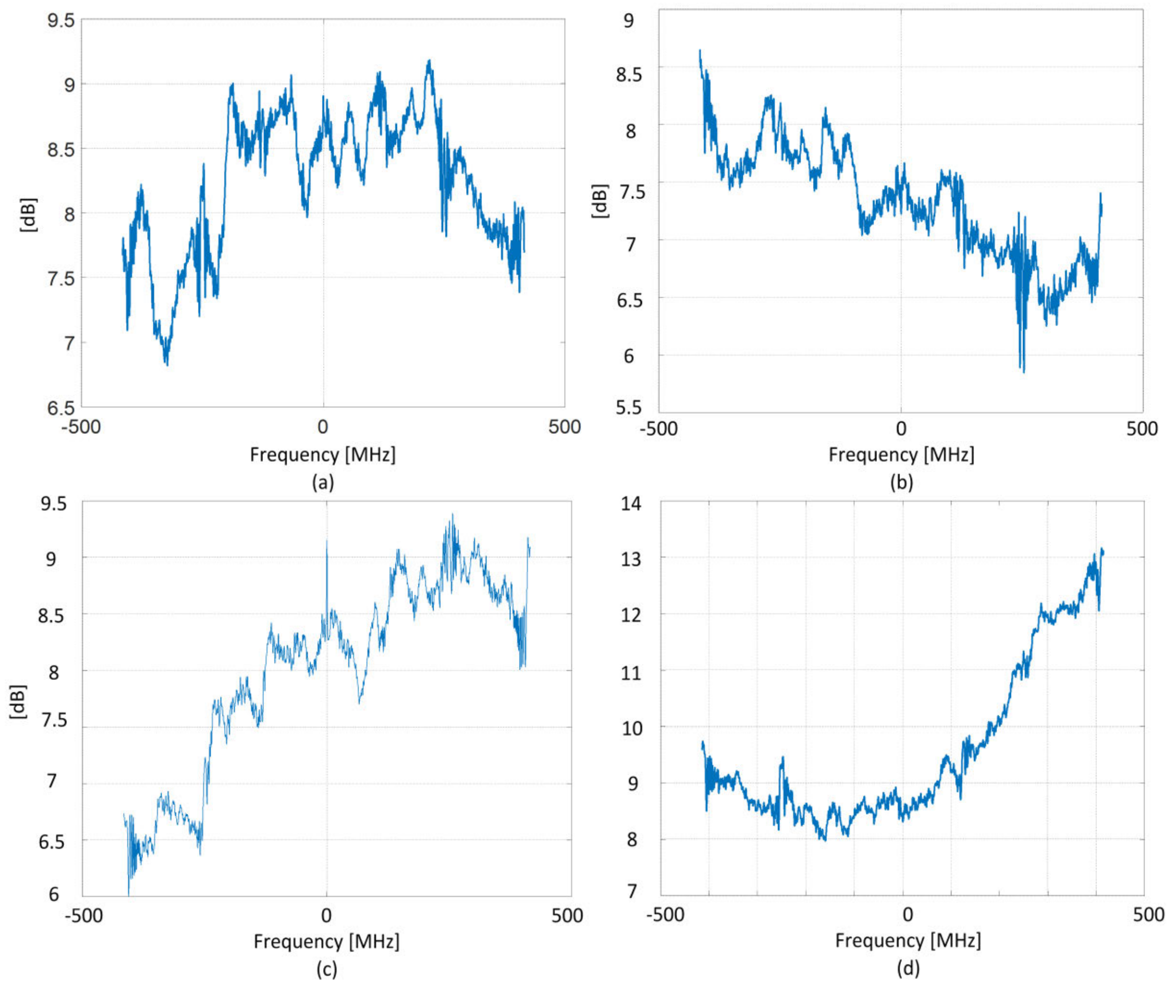

FIGURE 10. Amplitude frequency responses of term $\frac{H_{t\rightarrow r}}{Hk_{c\rightarrow r}} \cdot \frac{1}{Hk_{t\rightarrow c}} \cdot \frac{Hk_{coup1\text{-}2} \cdot Hk_{coup2\text{-}1}}{Hk_{coup1\text{-}3} \cdot Hk_{coup3\text{-}1}}$ associated with four transmit-receive calibration channel for subband1.

where H_{switch} and Hk_{switch} represent transfer functions from the transmitter output port and port3 of the kth coupler to the input port of RFU (as shown in the Capital letter X in Fig. 4), respectively; and $H_{RFU+FODU}$ is the combined transfer function of RFU and FODU.

As illustrated above, the reference and transmit calibration pulses are adjacent in time. And such a short time interval promises very little changes in the $H_{RFU+FODU}$ that this term in both numerator and denominator of Eq. (10) can be removed. Therefore, $\frac{H_{t\rightarrow r}}{Hk_{c\rightarrow r}}$ can be rewritten as

$$\frac{H_{t\rightarrow r}}{Hk_{c\rightarrow r}} = \frac{H_{switch}}{Hk_{switch}} \tag{11}$$

Due to the fact that both H_{switch} and Hk_{switch} only include switches, they will have stable performance during the whole mission and can thus be measured precisely before the integration of ICM.

To summarize, the final range replica can be obtained from signals of three calibration modes in combination with properties of couplers and that of switches within the ICM; otherwise it will not achieve satisfactory compression results. Since couplers and switches are all stable modules, they can be measured and determined in advance. Furthermore, susceptible effects of RFU and FODU in calibration routes can be effectively avoided by the subtle calibration sequences.

IV. AIRBORNE CAMPAIGN RESULTS

A. AIRBORNE TEST PLATFORM

To validate the effectiveness of internal calibration scheme for ultra-high resolution reflector SAR system, an airborne flight campaign was carried out. In this experiment, a three-axis Servo system, each of whose axes could be controlled independently, was employed to simulate the satellite attitude maneuvering in orbit. The airborne SAR antenna was a solid

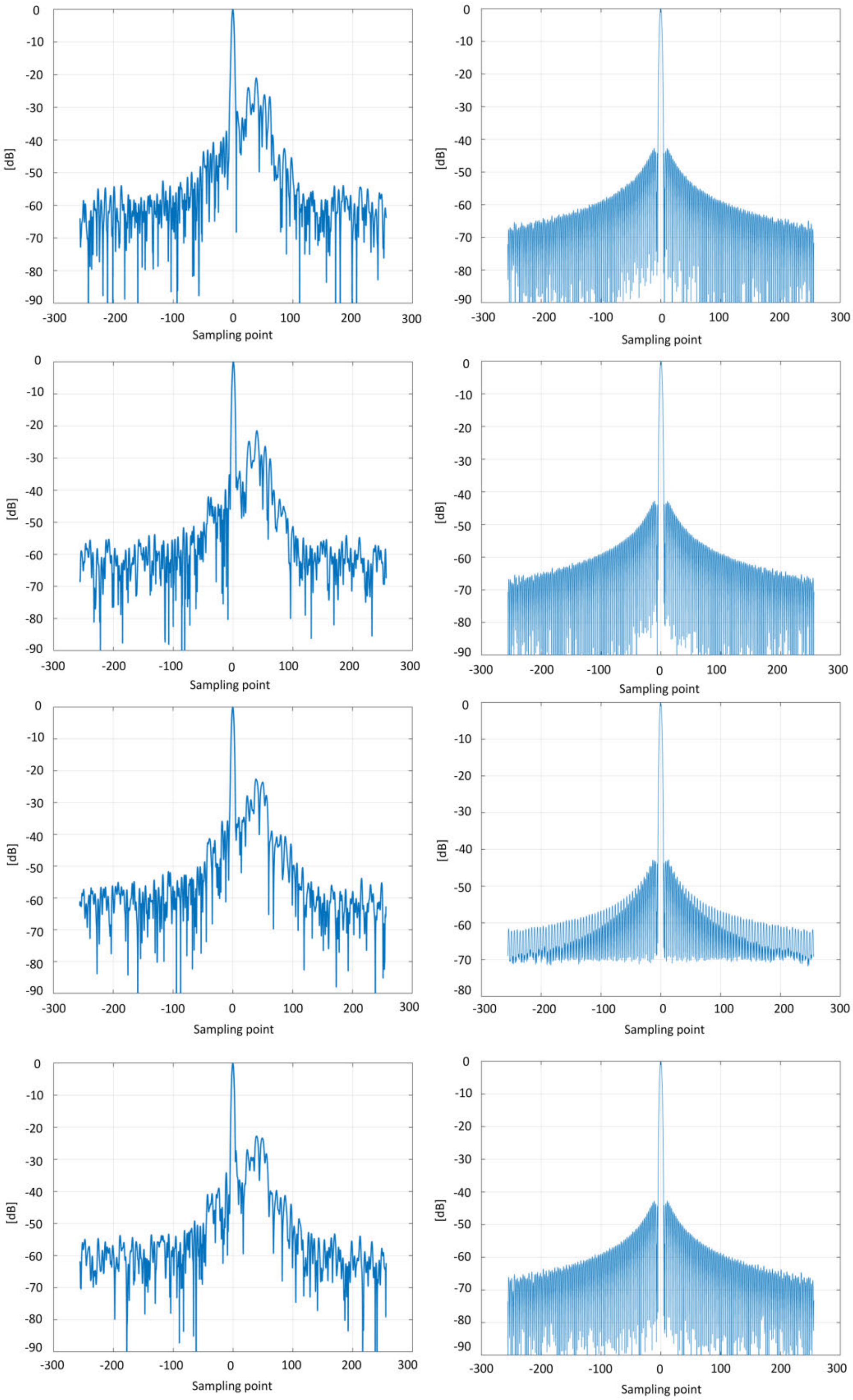

FIGURE 11. Range compression results between range replica and system closed-loop signals, and from top to bottom are results corresponding to subband1 ∼ subband4, respectively.

surface reflector connected to the Servo by which its beam scanning in azimuth could be realized mechanically, as seen in Fig. 8.

The airborne SAR worked at X-band, and the overall range bandwidth was 3.03 GHz consisting of four step subbands. The pulse transmission was in an alternate manner, the same as that in spaceborne SAR case. All the SAR system operation parameters are shown in Table 3.

B. INTERNAL CALIBRATION VERIFICATION RESULTS

In order to guarantee the image quality of airborne SAR experiment, effectiveness of internal calibration scheme were verified ahead of the flight. Taking subband1 as an example, amplitude-frequency responses associated with terms $\mathrm{H}k_{\mathrm{T}} \cdot \mathrm{H}k_{\mathrm{R}} / \mathrm{H}_{\mathrm{ref}}(\mathrm{k}=1,2,3,4)$ are shown in Fig. 9, where blue lines indicate the result obtained from single calibration cycle and red ones the average result of 1024 cycle repetitions. It can be seen that differences among $\mathrm{H}k_{\mathrm{T}} \cdot \mathrm{H}k_{\mathrm{R}} / \mathrm{H}_{\mathrm{ref}}(\mathrm{k}=1,2,3,4)$, due to the combined effects of transmit-receive loops, ICM, as well as couplers, are quite apparent. To compensate effects induced by ICM and coupler, the term $\frac{\mathrm{H}_{\mathrm{t}\rightarrow\mathrm{r}}}{\mathrm{H}k_{\mathrm{c}\rightarrow\mathrm{r}}} \cdot \frac{1}{\mathrm{H}k_{\mathrm{t}\rightarrow\mathrm{c}}} \cdot \frac{\mathrm{H}k_{\mathrm{coup1\text{-}2}} \cdot \mathrm{H}k_{\mathrm{coup2\text{-}1}}}{\mathrm{H}k_{\mathrm{coup1\text{-}3}} \cdot \mathrm{H}k_{\mathrm{coup3\text{-}1}}}$ (k = 1, 2, 3, 4) in Eq. (8) must be taken into account.

As described above in Section 3, each individual term within it could be measured and determined separately, and amplitude-frequency responses of this term associated with four internal calibration channels are given in Fig. 10. Due to the effect of voltage standing wave ratio (VSWR) [25], it clearly shows a severe amplitude variation of 2∼5 dB within the bandwidth of each subband. And if not compensated, this variation will cause distortion in the range compression results.

At last, we could attain the final range replica for subband1 with Eq. (8) and Eq. (9) based upon above results. And the same procedure could be applied to acquire replicas for other three subbands.

Figure 11 compares range compression results achieved by signals of transmit-receive loop and range replica before (left column) and after (right column) the term $\frac{\mathrm{H}_{\mathrm{t}\rightarrow\mathrm{r}}}{\mathrm{H}k_{\mathrm{c}\rightarrow\mathrm{r}}} \cdot \frac{1}{\mathrm{H}k_{\mathrm{t}\rightarrow\mathrm{c}}} \cdot \frac{\mathrm{H}k_{\mathrm{coup1\text{-}2}} \cdot \mathrm{H}k_{\mathrm{coup2\text{-}1}}}{\mathrm{H}k_{\mathrm{coup1\text{-}3}} \cdot \mathrm{H}k_{\mathrm{coup3\text{-}1}}}$ is introduced to compensate the phase and amplitude variation. By comparison, we can safely get to the point that much better performance had been realized only after extra terms caused by ICM and couplers being removed.

Then, spectra of these subbands were combined in frequency domain to achieve wider bandwidth and consequently higher range resolution with the approach in [26], [27]. Fig. 12 gives the compression result where Hamming window function is employed as used in subband compression, and corresponding performance parameters including impulse response width (IRW), peak sidelobe ratio (PSLR) and integrated sidelobe ratio (ISLR) are listed in Table 4.

Based on above analysis and obtained results, it can be concluded that the presented internal calibration scheme could successfully extract the effective range replica for each subband. And this paved the way for the following airborne flight experiment.

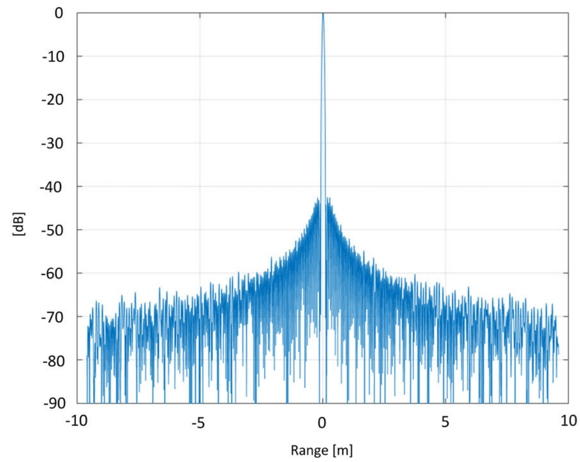

FIGURE 12. Range compression results after the combination of four subbands spectra.

TABLE 4. Performance parameters of range compression.

IRW	PSLR	ISLR
1.48	-42 dB	-26.5 dB

C. SAR IMAGING RESULTS

With finally acquired SAR images, three goals have been achieved in this airborne SAR campaign. The first one is multi-angle observation which can retrieve more information, as illustrated in Fig. 13.

This triangular roof is illuminated from three azimuth angles, namely +20 degrees (forward looking), 0 (boresight looking) and -20 degrees (backward looking) in the sliding spotlight mode. It can be seen that the same object shows quite different scattering properties under variant observation angles, as bright segment of roof gradually changes from left to right. This is due to the fact that roof section which approximately forms the mirror reflection and shows the highest brightness is varying during the data acquisition. Consequently, image fusion could be performed to manifest the object in a more comprehensive way, as shown in Fig. 14.

Secondly, the attitude maneuvering strategy, payload electronics configuration and corresponding internal calibration scheme are validated as a whole. Fig. 15 shows the SAR image of country area (5km in range × 4∼5 km in azimuth) acquired by sliding spotlight mode, in which inverted trapezoid contour is due to its corresponding imaging geometry.

Last but not least, a quantitative analysis is carried out to evaluate performance parameters. A triangular corner reflector, as shown in upper-half of Fig. 16, with 15cm side length is employed as a reference target and its correlative image is given in the red rectangle of lower-half.

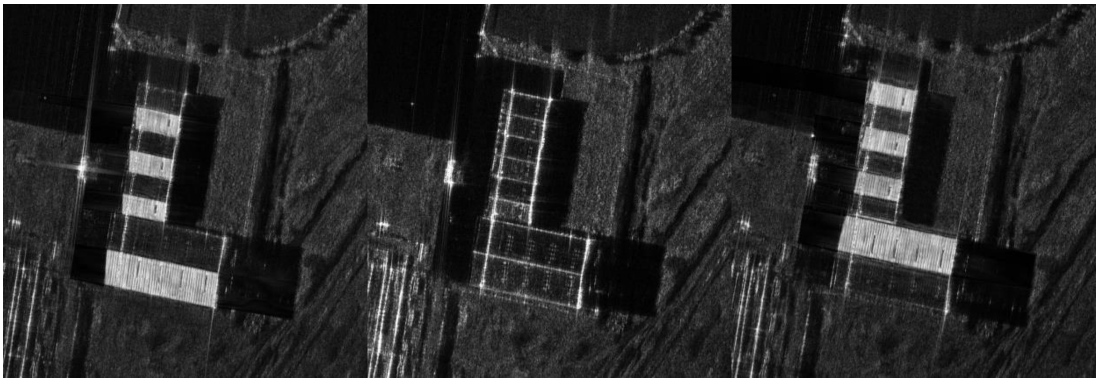

FIGURE 13. Imaging results of roof top from forward, boresight and backward azimuth observation angles.

FIGURE 14. Image fusion result of triangular roof from different azimuth observation angles.

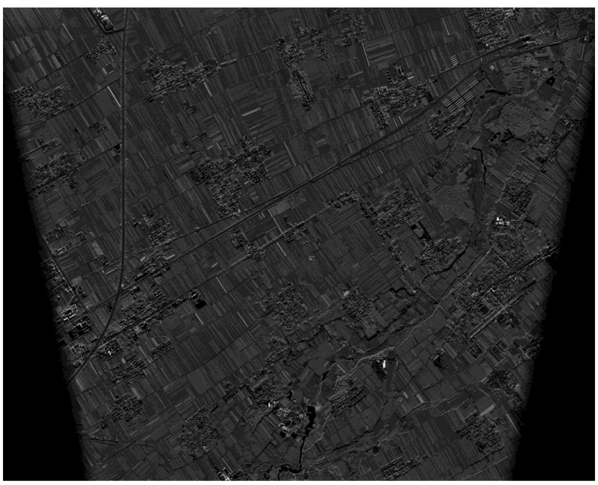

FIGURE 15. Airborne SAR images of sliding spotlight mode.

FIGURE 16. (Upper) triangular corner reflector and (lower) its corresponding SAR image in red square.

Two-dimensional interpolation is then implemented on this target area to quantitatively assess the precise resolution in both range and azimuth direction. Fig.17 presents the interpolation result and associated performance parameters are listed in Table 5, and these are in very accordance with initial system design and simulation objectives.

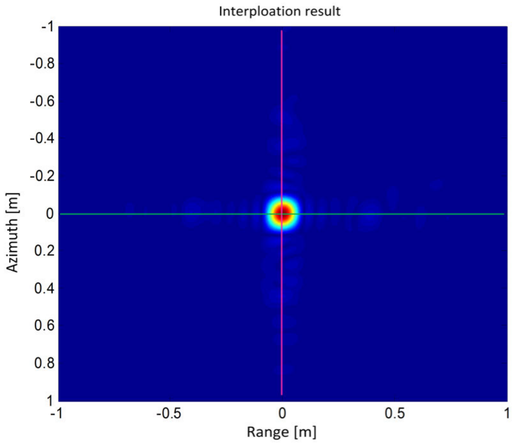

FIGURE 17. Two-dimensional interpolation result of reference target area.

TABLE 5. Two dimensional imaging performance of airborne SAR campaign.

	Parameters	Values
Ground range	resolution	0.0723m
	PSLR	-27.03 dB
	ISLR	-21.45 dB
Azimuth	resolution	0.0881m
	PSLR	-26.96 dB
	ISLR	-21.92 dB

V. CONCLUSION

To reap the potential benefits of spaceborne reflector SAR system, this paper puts forward an exemplary system which can realize ultra-high resolution and multi-angle observation in azimuth by satellite maneuvering. The maneuvering strategy which specifies the satellite attitude in terms of its three axes during imaging is proposed, thereby improving the efficiency of imaging processing. Then, the overall SAR payload electronics and each of its modules are present to illustrate the operation rationale. As one of key technique of this system, an innovative internal calibration scheme is suggested and described in detail to achieve objectives of imbalance correction and range replica extraction. In the end, an airborne flight campaign results are given to verify the effectiveness of reflector SAR as well as its internal calibration scheme in high resolution SAR imaging.

ACKNOWLEDGMENT

The authors would like to thank anonymous reviewers for their valuable comments and suggestions to improve the quality and readability of this article.

REFERENCES

[1] N. Gebert, "Multi-channel azimuth processing for high-resolution wide-swath SAR imaging," Ph.D. dissertation, Dept. Elect. Eng. Inf. Technol., Univ. Karlsruhe, Karlsruhe, Germany, 2009.

[2] M. Villano, "Staggered synthetic aperture radar," Ph.D. dissertation, Dept. Elect. Eng. Inf. Technol., Univ. Karlsruhe, Karlsruhe, Germany, 2016.

[3] A. Moreira, P. Prats-Iraola, M. Younis, G. Krieger, I. Hajnsek, and K. P. Papathanassiou, "A tutorial on synthetic aperture radar," *IEEE Geosci. Remote Sens. Mag.*, vol. 1, no. 1, pp. 6–43, Mar. 2013.

[4] F. Q. D. Almeida, "Multichannel staggered SAR for high-resolution wide-swath imaging," Ph.D. dissertation, Dept. Elect. Eng. Inf. Technol., Univ. Karlsruhe, Karlsruhe, Germany, 2017.

[5] T. Rommel, "Development, implementation, and analysis of a multiple-input multiple-output concept for spaceborne high-resolution wide-swath synthetic aperture radar," Ph.D. dissertation, Dept. Elect. Eng. Inf. Technol., Tech. Univ. Chemnitz, Chemnitz, Germany, 2018.

[6] A. R. Brenner, H. Essen, and U. Stilla, "Representation of stationary vehicles in ultra-high resolution SAR and turntable ISAR images," in *Proc. EUSAR*, Nuremberg, Germany, Apr. 2012, pp. 147–150.

[7] A. Reigber, R. Scheiber, M. Jager, P. Prats-Iraola, I. Hajnsek, T. Jagdhuber, K. P. Papathanassiou, M. Nannini, E. Aguilera, S. Baumgartner, R. Horn, A. Nottensteiner, and A. Moreira, "Very-high-resolution airborne synthetic aperture radar imaging: Signal processing and applications," *Proc. IEEE*, vol. 101, no. 3, pp. 759–783, Mar. 2013.

[8] J. C. Curlander and R. N. McDonough, *Synthetic Aperture Radar: Systems and Signal Processing*. New York, NY. USA: Wiley, 1991.

[9] I. G. Cumming and F. H. Wong, *Digital Processing of Synthetic Aperture Radar Data: Algorithms and Implementation*. Boston, MA, USA: Artech House, 2005.

[10] F. T. Ulaby and D. Long, *Microwave Radar and Radiometric Remote Sensing*. Ann Arbor, MI, USA: Univ. Univ. of Michigan Press, 2014.

[11] J. Mittermayer, S. Wollstadt, P. Prats-Iraola, and R. Scheiber, "The TerraSAR-X staring spotlight mode concept," *IEEE Trans. Geosci. Remote Sens.*, vol. 52, no. 6, pp. 3695–3706, Jun. 2014.

[12] P. Prats-Iraola, R. Scheiber, M. Rodriguez-Cassola, S. Wollstadt, J. Mittermayer, B. Brautigam, M. Schwerdt, A. Reigber, and A. Moreira, "High precision SAR focusing of TerraSAR-X experimental staring spotlight data," in *Proc. IEEE Int. Geosci. Remote Sens. Symp.*, Munich, Germany, Jul. 2012, pp. 3576–3579.

[13] T. Kraus, B. Brautigam, J. Mittermayer, S. Wollstadt, and C. Grigorov, "TerraSAR-X staring spotlight mode optimization and global performance predictions," *IEEE J. Sel. Topics Appl. Earth Observ. Remote Sens.*, vol. 9, no. 3, pp. 1015–1027, Mar. 2016.

[14] M. Younis, S. Huber, A. Patyuchenki, F. Bordoni, and G. Krieger, "Performance comparison of reflector- and planar-antenna based digital beam-forming SAR," *Int. J. Antennas Propag.*, vol. 2009, pp. 1–14, Jun. 2009.

[15] U. Steinbrecher, D. Schulze, J. Boer, and J. Mittermayer, "TerraSAR-X instrument operations rooted in the system engineering and calibration project," *IEEE Trans. Geosci. Remote Sens.*, vol. 48, no. 2, pp. 633–641, Feb. 2010.

[16] S. Buckreuss and B. Schattler, "The TerraSAR-X ground segment," *IEEE Trans. Geosci. Remote Sens.*, vol. 48, no. 2, pp. 623–632, Feb. 2010.

[17] H. Breit, T. Fritz, U. Balss, M. Lachaise, A. Niedermeier, and M. Vonavka, "TerraSAR-X SAR processing and products," *IEEE Trans. Geosci. Remote Sens.*, vol. 48, no. 2, pp. 727–740, Feb. 2010.

[18] R. J. Mailloux, *Phased Array Antenna Handbook*. Norwood, MA, USA: Artech House, 2005.

[19] R. C. Hansen, *Phased Array Antennas*. Hoboken, NJ. USA: Wiley, 2009.

[20] U. Naftaly and R. Levy-Nathansohn, "Overview of the TECSAR satellite hardware and Mosaic mode," *IEEE Geosci. Remote Sens. Lett.*, vol. 5, no. 3, pp. 423–426, Jul. 2008.

[21] H. Balzter, M. Davidson, and S. Quegan, "BIOMASS report for assessment," Eur. Space Agency, Harvard Univ., Cambridge, MA, USA, Tech. Rep. ESA SP 1313/2, 2008.

[22] P. Rosen, S. Hensley, S. Shaffer, W. Edelstein, Y. Kim, R. Kumar, T. Misra, R. Bhan, and R. Sagi, "The NASA-ISRO SAR (NISAR) mission dual-band radar instrument preliminary design," in *Proc. IEEE Int. Geosci. Remote Sens. Symp. (IGARSS)*, Fort Worth, TX, USA, Jul. 2017, pp. 3832–3835.

[23] S. Huber, F. Q. de Almeida, M. Villano, M. Younis, G. Krieger, and A. Moreira, "Tandem-L: A technical perspective on future spaceborne SAR sensors for earth observation," *IEEE Trans. Geosci. Remote Sens.*, vol. 56, no. 8, pp. 4792–4807, Aug. 2018.

[24] L. Li and F. Feng, "A satellite attitude maneuvering approach to realizing ultra-high resolution sliding spotlight imaging mode of spaceborne SAR," China Patent 106 291 557 B, Sep. 18, 2018.

[25] D. M. Pozar, *Microwave Engineering*, 4th ed. New York, NY. USA: Wiley, 2012.

[26] J. H. G. Ender and A. R. Brenner, "PAMIR—A wideband phased array SAR/MTI system," *IEE Proc., Radar Sonar Navig.*, vol. 150, no. 3, pp. 165–172, 3rd Quart., 2003.

[27] R. T. Lord, "Aspects of stepped-frequency processing for low-frequency SAR systems," Ph.D. dissertation, Dept. Elect. Eng., Univ. Cape Town, Rondebosch, South Africa, 2000.

LI LI was born in Shaanxi, China, in 1976. He received the B.S. degree in communications and iInformation systems from Xidian University, in 1998. He is currently pursuing the Ph.D. degree in electronics and information with Northwestern Polytechnical University. Since 1998, he has been with China Academy of Space Technology, Xi'an, China, where he was involved in the high speed data transmission and spaceborne remote sensing technology. He has been the vice Chief Designer of several GAO FEN series satellites of China, and the Leader of data transmission subsystem specifically. He has coauthored more than 20 articles and holds ten patents. His research interests include spaceborne remote sensing payload and data transmission system design.

MINGYI HE (Member, IEEE) received the B.Sc. and M.Sc. degrees from Northwestern Polytechnical University (NPU), Xi'an, China, in 1982 and 1985, respectively, and the Ph.D. degree from Xidian University, Xi'an, in 1994, all in electrical engineering. He has been with the School of Electronics and Information, NPU, where he is currently the Leading Professor for NPU signal and information processing. He is the Founder and Director of Shaanxi Key Laboratory of Information Acquisition and Processing and the Director and Chief Scientist of the Center for Earth Observation Research. He was a Visiting Professor with The University of Adelaide, Adelaide, Australia, and The University of Sydney, Sydney, Australia. He conducted a number of national projects and international joint research projects or joint graduate programs (such as Rockwell International Collins project in the USA, joint education programs and research with The University of Adelaide, and international Research and Development Center with MENSI, France). He has published more than 300 articles in the IEEE Transactions on Pattern Analysis and Machine Intelligence, the IEEE Transactions on Geoscience and Remote Sensing, the *International Journal of Computer Vision, Signal Processing, Signal Image and Video Processing, IET Image Processing, International Conference on Image Processing*, the IEEE Conference on Computer Vision and Pattern Recognition (CVPR), the IEEE China Summit and International Conference on Signal and Information Processing (ChinaSIP), and the International Conference on Industrial Engineering and Applications (ICIEA). He is the author or coauthor of five books (including *Digital Image Processing*: Science Press, 2008 and *Neural Network and Signal Processing Systems*: NPU Press, 1998). He has made valuable contributions to hyperspectral image processing, computer vision and image processing, neural networks and intelligent information processing with notable applications to X-ray image processing for luggage inspection and laser-finder test system for airborne systems. He has been a member of the Advisor Committee of China National Council for Higher Education on Electronics and Information, a member of the Chinese lunar exploration expert group, the Vice-President of Shaanxi Institute of Electronics, the Vice-Director of Spectral Imaging Earth Observation Committee of China Committee of International Society of Digital Earth, the Vice President of Space Remote Sensing Society (CSA), and the Vice-Chairman of The Institution of Engineering and Technology at Xi'an Network. He was the General Cochair of the IEEE ICIEA 2009, the Technical Program Committee Co-chair of the ICIEA 2013, and the General Chair of ChinaSIP 2014. He was the recipient of the IEEE CVPR 2012 Best Paper Award and is recognized as the "2012 Chinese Scientist of the Year" and was awarded ten scientific prizes from China and the governmental lifelong subsidy for outstanding contribution to higher education and scientific research by the State Council of China, since 1993.

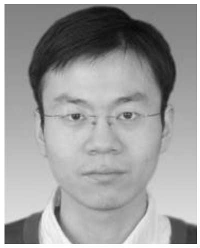

FAN FENG was born in Shaanxi, China, in 1984. He received the B.Sc. degree from the University of Science and Technology of China (USTC), Hefei, China, in 2006, and the Ph.D. degree from the Graduate University of Chinese Academy of Sciences (GUCAS), Beijing, in 2012. Since 2012, he has been with the China Academy of Space Technology, Xi'an, China, where he was involved in high resolution remote sensing technology. His research interests include spaceborne and airborne synthetic aperture radar (SAR) technology for advanced modes, SAR raw data simulation and SAR signal processing.

CAIPIN LI was born in 1984. He received the bachelor's degree from Air Force Engineering University and the master's degree from China Academy of Space Technology. He is interested in microwave remote sensing system technology, and SAR imaging technology.